Journal of The Electrochemical Society, **157** (2) B299-B307 (2010)
0013-4651/2009/157(2)/B299/9/$28.00 © The Electrochemical Society

Defect Chemistry and Thermomechanical Properties of $Ce_{0.8}Pr_xTb_{0.2-x}O_{2-\delta}$

C. Chatzichristodoulou,[a,b,z] P. V. Hendriksen,[a] and A. Hagen[a]

[a]*Fuel Cells and Solid State Chemistry Division, Risø DTU National Laboratory for Sustainable Energy, Technical University of Denmark, DK-4000 Roskilde, Denmark*
[b]*Niels Bohr Institute, University of Copenhagen, DK-2100 Copenhagen, Denmark*

The oxygen nonstoichiometry (δ) of $Ce_{0.8}Pr_xTb_{0.2-x}O_{2-\delta}$ ($x = 0, 0.05, 0.10, 0.15, 0.20$) was measured as a function of P_{O_2} at temperatures between 600 and 900°C by coulometric titration and thermogravimetry. A nonideal solution model, allowing for a linear δ dependence of the partial molar enthalpy of reduction in the dopants, could successfully reproduce the experimentally determined oxygen nonstoichiometry. X-ray absorption near-edge spectroscopy measurements were performed at the Ce/Pr/Tb L3 and L2 edges. The valence state of each dopant was affected by the presence of the co-dopant. The redox properties strongly depended on the lattice strain energy and the mean metal–oxygen bond strength. The thermal and chemical expansion coefficients were determined by dilatometry. The strongly nonlinear behavior of the thermal expansion coefficient originated from the chemical strain due to increasing oxygen nonstoichiometry with increasing temperature.
 [DOI: 10.1149/1.3270475]

Manuscript received July 15, 2009. Published December 29, 2009.

Significant scientific effort has been devoted to the study of ceria-based oxides, as they exhibit transport and catalytic properties that render them appropriate for a variety of applications, such as electrolytes and electrodes for solid oxide fuel cells (SOFCs),[1] three-way catalysts,[2] oxygen sensors,[3] and oxygen permeation membranes.[4]

Fast oxide ion conduction can be achieved by the introduction of oxide ion vacancies, for example, as a result of charge compensation when substituting Ce^{4+} with lower valency cations (e.g., Gd^{3+} or Ca^{2+}). The oxygen nonstoichiometry (δ) of pure and doped ceria increases with decreasing oxygen partial pressure and increasing temperature, accompanied by partial reduction of Ce^{4+} to Ce^{3+}. This induces electronic conductivity, which takes place via a small polaron hopping mechanism.[5-9] The electronic conductivity limits the use of the material as an electrolyte for SOFCs at low temperatures (500–600°C) [10] but makes it attractive for applications where mixed ionic–electronic conduction is required. Mixed conduction in ceria can be extended to a broader P_{O_2} range by doping with multivalent cations, such as Pr or Tb, both of which can have a mixed (3 + /4 +) valence state. This has enhanced the electronic conductivity of ceria within the high P_{O_2} regime (10^{-5}–10^{-1} atm).[11-16]

The solubility limit of Pr in ceria has been assessed by X-ray diffraction (XRD) to be 30 atom %.[12,17] The oxygen nonstoichiometry of the 20 atom % Pr-doped ceria has been previously investigated in the high P_{O_2} regime over the temperature ranges of 800–950°C (for microcrystalline powder)[18] and 600–750°C (for nanocrystalline powder)[11] by coulometric titration (CT). In both cases, a simple defect model treating the reduction of Pr^{4+} to Pr^{3+} in an ideal manner [i.e., not allowing the partial molar enthalpy for oxygen incorporation (h_O–h_O^o) to vary with the degree of nonstoichiometry] accounted well for the nonstoichiometry data. We have presented the oxygen nonstoichiometry and defect chemistry of microcrystalline $Ce_{0.8}Pr_{0.2}O_{2-\delta}$ in a previous publication.[19] A nonideal solution model with linear δ dependency of h_O–h_O^o for the reduction of Pr (called linear δ for simplicity) was necessary to reproduce the δ(log P_{O_2}) curves in the entire nonstoichiometry range examined at each temperature.

Various examples of a nonideal reduction behavior exist in the literature; The reduction of the perovskite compounds $La_{1-x}Sr_xCrO_{3-\delta}$ [20] and $La_{1-x}Sr_xCoO_{3-\delta}$ [21] has also been observed to follow a regular solution behavior (which for small δ corresponds to a linear dependence of h_O–h_O^o on δ). For $La_{1-x}Ca_xCrO_{3-\delta}$, a linear relationship should be expected between the excess standard Gibbs energy change (ΔG_{exc}^o) and δ based on the estimation of pair potential changes due to the defect-induced lattice expansion.[22] The deviation of the redox energetics of $SrFeO_{3-\delta}$ from ideality could be successfully interpreted by an excess term of purely configurational entropic origin.[23]

Oxygen loss upon heating in air gives rise to a highly nonlinear thermal expansion coefficient (TEC) ranging between 10×10^{-6} and 36×10^{-6} K^{-1} over the temperature range of 30–1000°C.[16,18] The effect of co-doping Pr-doped ceria with either Gd [18] or Zr [12,24] on δ and TEC has also been investigated. Co-doping with 15 atom % Gd caused a decrease in the fractional concentration of Pr^{4+}, leading to smaller changes in δ and therefore slightly smaller TEC values. The value of h_O–h_O^o decreased from 73 ± 6 to 42 ± 4 kJ/mol, resulting in a more facile reduction of Pr. Co-doping with 10 atom % Zr also increased the fractional concentration of Pr^{3+} and substantially decreased the TEC to values between 13×10^{-6} and 18×10^{-6} K^{-1} in the temperature range of 30–1000°C.

Tb is soluble in ceria to even higher amounts than Pr, exceeding 50 atom %.[25-28] No thorough study on the oxygen nonstoichiometry of Tb-doped ceria has been performed so far. X-ray absorption near-edge spectroscopy (XANES) measurements at the Tb L3 edge on samples with various amounts of Tb doping, published by three different groups,[15,28,29] have indicated an increase in the fractional concentration of Tb^{4+} with increasing Tb amount. The TEC of nanocrystalline Tb-doped ceria determined by high temperature XRD in the temperature range of 25–800°C decreased from 11.7×10^{-6} to 10.8×10^{-6} K^{-1} with increasing Tb content from 0 to 30 atom %.[15] Co-doping with Zr yielded unexpectedly high concentrations of Tb^{3+}, which is not seen in $TbO_{2-\delta}$ or $Ce_{1-x}Tb_xO_{2-\delta}$.[30] Density functional calculations indicated a significant change in the energetics for the removal of O, from being a highly endothermic process for pure ceria to becoming slightly exothermic for the ternary oxide. It should be stressed though that in the ternary oxide the expulsion of O is related to reduction of Tb and not Ce, Tb being intrinsically more easily reduced than Ce. However, stabilization of the tetravalent state of Tb was observed when co-doping with Ca.[31]

In this contribution, samples of ceria doped with Pr and Tb are examined. CT and thermogravimetry (TG) are used to determine the oxygen nonstoichiometry over a wide P_{O_2} range, covering both the reduction of Pr/Tb and Ce, at temperatures between 600 and 900°C. The defect chemistry of these materials is modeled with a δ-linear solution approach for the reduction in the dopants. Thermodynamic parameters determining the redox behavior are determined and discussed with respect to their compositional dependence. XANES

[z] E-mail: ccha@risoe.dtu.dk

measurements have been performed to estimate the valence state of each cation and to investigate the effect of co-doping on the redox properties of the two elements in the ceria lattice. Finally, the thermal and chemical expansion coefficients of $Ce_{0.8}Pr_xTb_{0.2-x}O_{2-\delta}$ are determined.

Experimental

Sample preparation and phase analysis.— Powders of $Ce_{0.8}Pr_xTb_{0.2-x}O_{2-\delta}$ with $x = 0$, 0.05, 0.10, 0.15, 0.20 were synthesized by coprecipitation. Aqueous solutions of $Ce(NO_3)_3 \cdot 6H_2O$ (Alfa Aesar, 99.99%), $Pr(NO_3)_3 \cdot xH_2O$ (Alfa Aesar, 99.9%), and $Tb(NO_3)_3 \cdot 5H_2O$ (Johnson Matthey, 99.9%) were prepared. The solution concentrations were determined gravimetrically and by titration. Appropriate amounts of each solution were mixed in a glass container at 200°C. Coprecipitation of the metal oxalates was achieved by adding oxalic acid (1 M) while stirring the solution. The solutions were dried overnight at 300°C, and the resulting powders were calcined at 600°C. The powders were shaped into disks at a uniaxial pressure of 3 MPa and further isostatically compressed at a pressure of 325 MPa. The disks were sintered at 1500°C in air for 12 h and slowly cooled to room temperature at a rate of 0.5 K/min.

Phase analysis was performed by room-temperature XRD using a Bruker D8 Advance diffractometer with Cu Kα radiation and a LynxEye position sensitive detector. The diffractograms were recorded at the 2θ range of 20–80° with a step of 0.02° using a scan rate of 1 s/step. Unit cell parameters were determined by whole pattern Rietveld refinement using Fullprof.[32]

XANES.— As-sintered disks were further annealed at 800°C in air for 12 h and were quenched to room temperature in air. These samples are hereafter denoted as Q800CAir (quenched from 800°C in air). Approximately 5 mg of the powdered quenched disks was thoroughly mixed with 50 mg of cellulose in a mortar and was subsequently pressed into disks. XANES measurements at the Ce/Pr/Tb L3 and L2 edges were performed in the transmission mode at HASYLAB/DESY [extended X-ray absorption fine structure (EXAFS) E4 beamline] at room temperature and at a pressure of 10^{-9} atm using a Si(111) double-crystal monochromator at 40% detuning to suppress harmonics. A metal foil reference was used with each sample to accurately calibrate and align the energy scale for all spectra. In the near-edge region, equidistant energy steps of 0.2 eV were used. The intensity of the monochromatic X-ray beam was measured by three consecutive ionization chambers filled with argon and nitrogen at appropriate pressures. Leaking of the incident beam through parts of the sample having a less absorbent material results in an amplitude reduction in the XANES signal and an apparent shift of the absorption edge to lower energies.[33,34] To minimize the effects of sample inhomogeneity, we scanned the X-ray beam along the diameter of the disk and carefully selected a region of homogeneous absorption. The analysis of the XANES spectra was performed with IFEFFIT program package Athena.[35] All absorption spectra were normalized in the following manner. The background fitted below the edge was extrapolated by a linear function and was subtracted. The spectra were then normalized to unity by a linear function fitted in the EXAFS region and extrapolated to the edge.

Two series of reference samples, one with fully oxidized dopants and one with fully reduced dopants (Pr/Tb), were prepared by annealing samples of $Ce_{0.8}Pr_{0.2}O_{2-\delta}$ and $Ce_{0.8}Tb_{0.2}O_{2-\delta}$ under appropriate conditions. To obtain the oxidized reference samples, powders of as-sintered disks were annealed at 500°C in pure O_2 at a pressure of 40 atm for 2 days, and furnace cooled to room temperature in the same environment. For the fully reduced reference samples, sintered disks were annealed in a gas mixture of 0.4% H_2 + 79.6% N_2 + 20% H_2O at 800°C for 10 h, 700°C for 20 h, and 600°C for 40 h, defining a P_{O_2} of 10^{-21} atm at 600°C and finally cooled to room temperature in the same gas mixture at a rate of 5 K/min. These reference samples are hereafter denoted Oxidized and Reduced, respectively.

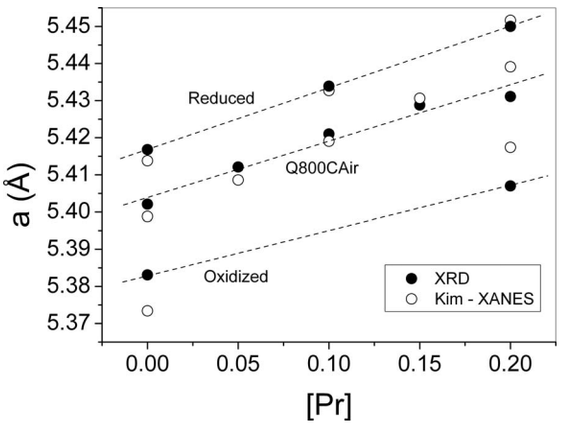

Figure 1. Lattice constant of $Ce_{0.8}Pr_xTb_{0.2-x}O_{2-\delta}$ as a function of composition after annealing at different conditions and comparison with values estimated from Kim's empirical relation.[36] The dashed lines serve as a guide for the eyes.

CT and TG.— As-sintered disks were crushed into powders, examined for phase purity by XRD, and used for CT and TG. A small alumina cup with a known mass of sample powder (~2 g) was fitted in a $Zr_{0.85}Y_{0.15}O_2$ (YSZ) cup covered with a YSZ lid and sealed with glass at 1000°C. The contact surfaces between the YSZ cup and the lid were polished using SiC paper and 3 μm diamond paste, and external uniaxial pressure was applied on the system to ensure a good seal. Four electrodes (two at the inner surface and two at the outer surface of the YSZ cup) served as working electrodes for the electrochemical pumping of oxygen and as reference electrodes for the determination of the P_{O_2} inside the cup. Pt paste was used for the reference electrodes. A thin (~10 μm) sprayed layer of $YSZ/La_{0.8}Sr_{0.2}MnO_3$ cermet covered with Pt paste was used for the working electrodes. A detailed description of the CT measurements can be found elsewhere.[19]

TG was performed using both a NETZSCH STA 409CD thermogravimeter and a NETZSCH TG 439 thermobalance. The P_{O_2} of the sample atmosphere was varied by appropriate gas mixtures (of air, N_2, and H_2) at a constant temperature and was measured downstream with a YSZ P_{O_2} sensor. After each gas change, the sample was left to equilibrate for 2 h. The measured weight loss was corrected for buoyancy effects using an alumina powder reference sample of the same volume measured under identical conditions.

Dilatometry.— The thermal and chemical expansion coefficients were estimated from dilatometry measurements performed with a NETZSCH DIL 402CD differential dilatometer with a sample load of 0.3 N. The thermal expansion of the sample rods was measured in air (100 mLn/min) by heating the samples from room temperature to 1000°C at a rate of 1 K/min. The samples were then cooled to 800°C, where the chemical expansion coefficient was determined, by varying the P_{O_2} of the sample atmosphere while keeping the temperature constant. The P_{O_2} control and monitoring were undertaken as described for the TG measurements. An Al_2O_3 rod measured simultaneously with the sample rod served as a standard for the calibration of the instrument.

Results and Discussion

A single fluorite phase was observed by room-temperature XRD, for all compositions and annealing conditions, indicating a solid solution of the dopants in the lattice of ceria in all cases. The lattice constants were determined by Rietveld refinement of the X-ray diffractograms. The variation in the lattice parameter with composition and annealing conditions is shown in Fig. 1. The lattice parameter increases upon reduction and with increasing relative amount of Pr,

as expected from the increase in the mean ionic radius of the dopants. An empirical relation was published by Kim,[36] relating the lattice constant of ceria with the ionic radii and the oxidation state of the dopants

$$a = 0.5413 + \sum_k (0.0220\Delta r_k + 0.00015\Delta z_k)m_k \quad [1]$$

where a (nm) is the lattice constant of the ceria solid solution at room temperature, Δr_k (nm) is the difference in the ionic radius ($r_k - r_{Ce}$) of dopant "k" and the Ce^{4+} radius in the eightfold coordination taken from Shannon,[37] Δz_k is the valence difference ($z_k - 4$), and m_k is the mole percent of the kth dopant in the form of MO_x.

The determined lattice parameters compare well with those predicted from Kim's empirical relation (Eq. 1) using the tetravalent fraction of each dopant determined by XANES (presented later). The lattice constant obtained from Kim's relation is slightly underestimated for Tb-rich compositions and slightly overestimated for Pr-rich compositions, especially for the Oxidized samples. This could be because Kim's relation has been derived from the data of lattice constant variation as a function of trivalent dopant concentration.[36]

Oxygen nonstoichiometry and defect chemistry.— The oxygen nonstoichiometry and defect chemistry of $Ce_{0.8}Pr_{0.2}O_{2-\delta}$ have been discussed in detail in a previous publication.[19] The reduction of Pr could not be modeled in an ideal manner [constant standard enthalpy (ΔH^o_{Pr}) and standard entropy (ΔS^o_{Pr}) of reduction], even with an additional defect reaction taking into account the association of reduced Pr species and oxygen vacancies. However, a nonideal solution model with a linear δ dependency of ΔH^o_{Pr} for the reduction of Pr (δ-linear model) could accurately reproduce the δ(log P_{O_2}) curves in the entire nonstoichiometry range examined and at all temperatures, at the same time yielding a δ dependence of the Gibbs energy of formation (ΔG_f) and the partial molar enthalpy ($h_O - h^o_O$) and entropy ($s_O - s^o_O$), which agrees with the one determined directly from the nonstoichiometry data. Because a similar defect formation behavior can be expected for the compounds $Ce_{0.8}Pr_xTb_{0.2-x}O_{2-\delta}$, a δ-linear solution model for the reduction of the dopants was adopted for the defect modeling of these compounds.

The δ-linear solution model includes for the reduction reaction of the dopants, M = Pr/Tb, an excess enthalpic term, linear with respect to δ

$$\Delta H^o_M = \Delta H^o_{M,\delta=0} + \Delta H^o_{M,exc} = \Delta H^o_{M,\delta=0} + a_H\delta \quad [2]$$

where the parameter a_H represents the rate of change in the partial molar enthalpy for the reduction of the dopants with oxygen nonstoichiometry, $d\Delta H^o_M/d\delta$. The defect formation reactions and equilibrium constants (K) using the Kröger–Vink notation for the point defects are

$$O^x_O + 2M^x_{Ce} \leftrightarrow \tfrac{1}{2}O_2(g) + V^{\bullet\bullet}_O + 2M'_{Ce}$$

$$K^{reg}_M = \exp\left(-\frac{\Delta H^o_{M,\delta=0} + \Delta H^o_{M,exc} - T\Delta S^o_M}{RT}\right) = \frac{P^{1/2}_{O_2}\cdot[V^{\bullet\bullet}_O]\cdot[M'_{Ce}]^2}{[O^x_O]\cdot[M^x_{Ce}]^2} \quad \Delta H^o_{M,\delta=0}, a_H, \Delta S^o_M = \text{const} \quad [3]$$

$$O^x_O + 2Ce^x_{Ce} \leftrightarrow \tfrac{1}{2}O_2(g) + V^{\bullet\bullet}_O + 2Ce'_{Ce}$$

$$K_{Ce} = \exp\left(-\frac{\Delta H^o_{Ce} - T\Delta S^o_{Ce}}{RT}\right) = \frac{P^{1/2}_{O_2}\cdot[V^{\bullet\bullet}_O]\cdot[Ce'_{Ce}]^2}{[O^x_O]\cdot[Ce^x_{Ce}]^2} \quad \Delta H^o_{Ce}, \Delta S^o_{Ce} = \text{const} \quad [4]$$

The mass (Eq. 5), site (Eq. 6 and 7), and charge (Eq. 8) conservation conditions can be written as

$$[M^x_{Ce}] + [M'_{Ce}] = 0.2 \quad [5]$$

$$[Ce^x_{Ce}] + [Ce'_{Ce}] + [M^x_{Ce}] + [M'_{Ce}] = 1 \quad [6]$$

$$[O^x_O] + [V^{\bullet\bullet}_O] = 2 \quad [7]$$

$$2[V^{\bullet\bullet}_O] = [M'_{Ce}] + [Ce'_{Ce}] \quad [8]$$

Five variables, $\Delta H^o_{M,\delta=0}$, a_H, ΔS^o_M, ΔH^o_{Ce}, and ΔS^o_{Ce}, were used for the fitting of the oxygen nonstoichiometry data with the δ-linear solution model at all temperatures. A sequential method[38] was adopted for the nonlinear least-squares fitting in all cases, allowing for the simultaneous contribution of all defect species in the defect equilibrium throughout the whole range, avoiding the use of Brouwer-type approximations.[39] The reduction of Pr and Tb in the co-doped compositions is not treated separately though, as they both occur within the same P_{O_2} range, making it impossible to distinguish between them. In all δ(log P_{O_2}) curves, a clear "plateau" is observed when $[M'_{Ce}] = 0.2$. Absolute values for the oxygen nonstoichiometry were obtained by adjusting the δ value at the minimum slope, $d\Delta\delta/dP_{O_2}$, of the observed plateau to 0.1, corresponding to a complete reduction of the dopants, Ce remaining in the fully oxidized state, as evidenced from the XANES results (see XANES subsection in the Results and Discussion section). Sequentially solving the set of linear and nonlinear equations describing the defect model yields a prediction for the P_{O_2} of each measured value of δ. Because the δ values close to the plateau suffer a much greater uncertainty in the determination of their corresponding P_{O_2}, the fitting was performed by weighting the square deviation by a factor of $|0.1 - \delta|$ in all cases.

Oxygen nonstoichiometry data for the compounds $Ce_{0.8}Pr_xTb_{0.2-x}O_{2-\delta}$, determined by CT and TG, together with the fits obtained with the δ-linear solution defect model, are shown in Fig. 2a-c for 600, 700, and 800°C, respectively. The δ-linear solution model is able to reproduce the P_{O_2} dependence of δ over the entire P_{O_2} range examined at each temperature for all compositions. At the oxygen nonstoichiometry regime related to the reduction of the dopants and at low temperatures, the Pr-rich compounds have a higher oxygen content (smaller oxygen nonstoichiometry) and are observed to release oxygen easier than the Tb-rich compounds with decreasing P_{O_2}, as can be seen at the insets of Fig. 2a and b. For values of δ above 0.08, the δ(log P_{O_2}) behavior of the dopants becomes almost identical for all compositions. This is the reason why at temperatures above 800°C it is not possible to distinguish between the reduction behaviors of the dopants for the various compositions. In the oxygen nonstoichiometry regime related to the reduction of Ce, the Pr-rich compounds start reducing at slightly higher P_{O_2} values than the Tb-rich ones.

The thermodynamic parameters, deduced from the fitting of the oxygen nonstoichiometry data of each composition with the δ-linear solution model, are listed in Table I. The parameters obtained for the partial molar enthalpy of reduction are plotted as a function of composition in Fig. 3a and b for the dopants and Ce, respectively. The positive sign of the partial molar enthalpies of reduction of both the dopants and Ce indicates that the expulsion of oxygen is an endothermic process.

The partial molar enthalpy for the reduction of the dopants at the fully oxidized state, $\Delta H^o_{M,\delta=0}$, increases with increasing Pr concentration; i.e., the reduction of Tb^{4+} to Tb^{3+} demands less heat than the

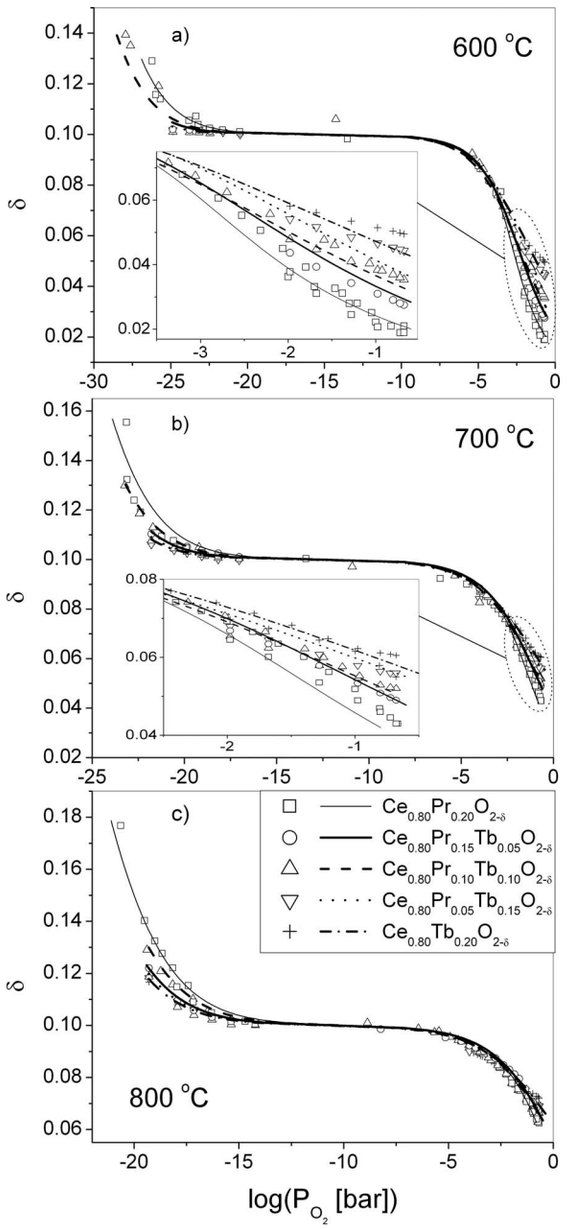

Figure 2. Oxygen nonstoichiometry and fit of the δ-linear solution defect model for the compounds $Ce_{0.8}Pr_xTb_{0.2-x}O_{2-\delta}$ at (a) 600, (b) 700, and (c) 800°C.

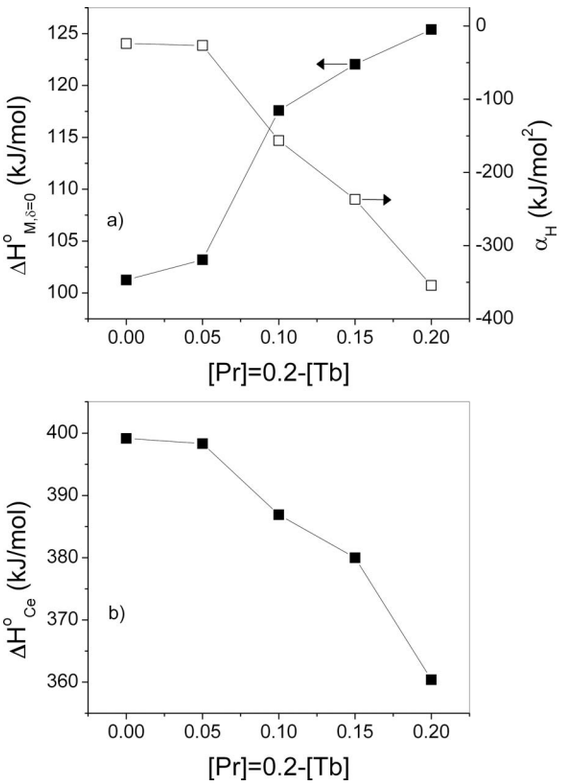

Figure 3. δ-linear solution model parameters for the partial molar enthalpy of reduction as a function of composition.

reduction of Pr^{4+} to Pr^{3+} in the lattice of ceria. The difference might arise from lattice strain energy due to the host–dopant mismatch. As discussed in reference to the XANES results, this contribution plays a significant role in the determination of the redox properties of the dopants. The ionic radius of Pr^{4+} is only slightly smaller than that of Ce^{4+}, whereas that of Tb^{4+} is significantly smaller. The reduction of Tb^{4+} to Tb^{3+} at the strongly oxidized state would lead to a significant reduction of the lattice strain, whereas the reduction of Pr^{4+} to Pr^{3+} might even result in a slight increase in the lattice strain energy as Pr^{3+} has a significantly larger ionic radius than Ce^{4+}. Values for the ionic radii discussed here are given in Table II.[37]

The value of the nonideality parameter, a_H, is almost zero for the Tb-rich compositions and decreases fast with increasing Pr content to large negative values, as shown in Fig. 3a. This results in a more facilitated expulsion of oxygen with increasing oxygen nonstoichiometry (Eq. 2) for the Pr-rich compositions in the oxygen nonstoichiometry regime related to the reduction of the dopants. We attribute this to a decrease in the strength of the metal–oxygen bond with decreasing oxidation state and increasing ionic radii of the cations. However, the Tb-rich compositions appear to behave in an ideal manner.

The reason for the different reduction behaviors of Pr and Tb in the lattice of ceria is not clear. It should be stressed though that the presence of two counteracting δ dependencies on a_H, canceling out and therefore resulting in an apparent ideal behavior for the Tb-rich compounds, cannot be excluded.

Table I. Thermodynamic parameters obtained from the fitting of the oxygen nonstoichiometry with the δ-linear solution model.

[Pr] = 0.20 − [Tb]	$\Delta H^o_{M,\delta=0}$ (kJ/mol)	a_H (kJ/mol^2)	ΔS^o_M (J/K mol)	ΔH^o_{Ce} (kJ/mol)	ΔS^o_{Ce} (J/K mol)
0.20	125	−354	69	360	91
0.15	122	−237	76	380	99
0.10	118	−156	76	387	111
0.05	103	−27	73	398	114
0.00	101	−24	72	399	113

Table II. Ionic radii for eightfold coordination.[37]

Ion	Radius (Å)
Ce^{4+}	0.97
Ce^{3+}	1.143
Pr^{4+}	0.96
Pr^{3+}	1.126
Tb^{4+}	0.88
Tb^{3+}	1.04
Zr^{4+}	0.84
Ca^{2+}	1.12

The value of the standard entropy change for the reduction reaction of the dopants is very similar for all compounds, at 69–76 J/K mol, as shown in Table I. The larger $d\delta/d$ log P_{O_2} slope observed in Fig. 2a and b for the Pr-rich compositions is the result of the increased nonideal behavior of these compounds relative to the Tb-rich ones, leading to a decreasing partial molar enthalpy of reduction with increasing δ and therefore to a more facilitated expulsion of oxygen and increasing slope $d\delta/d$ log P_{O_2}.

Both the partial molar enthalpy and the standard entropy for the reduction of Ce decrease with increasing Pr concentration. This leads to the observed more facilitated expulsion of oxygen for the Pr-rich compositions in the oxygen nonstoichiometry range related to the reduction of Ce. The difference among the various compositions decreases with increasing temperature due to the increasing entropic contribution for the Tb-rich compositions.

XANES.— The L3 white lines of Pr, Tb, and Ce are shown in Fig. 4a-c, respectively. A clear shift of the absorption edges to lower energies is observed in Pr and Tb upon reduction, indicating a decrease in the value of their valence state, whereas no change can be detected for Ce. This means that any change in δ within the P_{O_2} range defined by the annealing conditions for the Oxidized and Reduced samples should be attributed to the reduction of the dopants. Double-peaked white lines are observed in all cases, apart from the Pr and Tb edges of the Reduced samples, which agree with the L2 and L3 near-edge spectra generally observed in rare-earth (RE) ions.[40-42] Peak A arises from a transition of a 2p core electron from the $4f^n$ (RE^{4+}) initial configuration to the crystal field split 5d empty states. Peak B is the sum of two transitions from two initial configurations with different valences: $4f^{n+1}$ (RE^{3+}) and $4f^{n+1}L$ (RE^{4+}), where n = 0, 1, and 7 for Ce, Pr, and Tb, respectively. Therefore, the ratio of the integrated intensities of the two peaks can only provide an indication and not a direct measure of the valence state of each cation.

To examine whether reoxidation of Pr or Tb might occur at room temperature, which would imply that quenching of the samples is not effective, XANES spectra at the L2 edge of Pr and Tb recorded a few days after quenching and 6 months later were compared. The comparison for Pr depicted in Fig. 4d shows a small decrease in the ratio of the integrated intensities of peaks B and A, indicating a slight reoxidation of the sample. Quantifying this decrease (as described later) would yield a change of around 5% in the valence state of Pr over the period of 6 months, indicating that a very slow reoxidation of Pr^{3+} might occur at room temperature. This very small value (being close to the uncertainty of the measurement), as well as the fact that no change was observed in Tb, allows us to assume that the samples remain in the quenched state at room temperature over a sufficiently long period of time not to invalidate our results. The oxygen nonstoichiometry of the Q800CAir samples ($\delta \approx 0.065$, as determined from the total tetravalent dopant fraction, Fig. 6), which agrees with the equilibrium value at 800°C shown in Fig. 2, is also indicative of a successful quenching. Finally, the absence of peak A in the Pr and Tb spectra of the Reduced samples indicates the complete reduction of the dopants. This shows that the reduced state of Pr and Tb is indeed preserved by quenching.

Various methods for obtaining semiquantitative or even quantitative information for the oxidation state of the element in question from the absorption spectra have been suggested in the literature.[42-47] Principal component analysis and linear combination (LC) of XANES reference spectra to fit the experimental spectrum[45-47] were selected here as these approaches have proven to be reliable and sensitive tools for the determination of the type and relative amount of each component that contributes to the absorption spectrum of multicomponent systems, when the absorbance spectrum of each individual component significantly differs, and when proper reference compounds with similar structures, compositions,

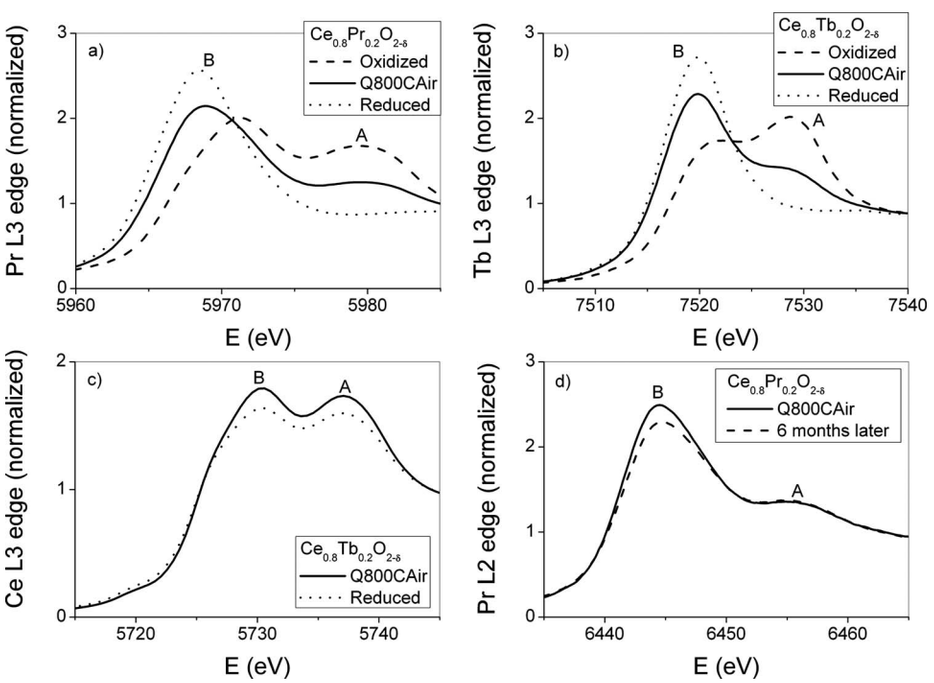

Figure 4. L3 absorption edges of (a) Pr, (b) Tb, and (c) Ce for oxidized, quenched from 800°C in air, and reduced samples and (d) L2 absorption edges of Pr for $Ce_{0.8}Pr_{0.2}O_{2-\delta}$ quenched from 800°C in air measured 3 days after quenching and 6 months later.

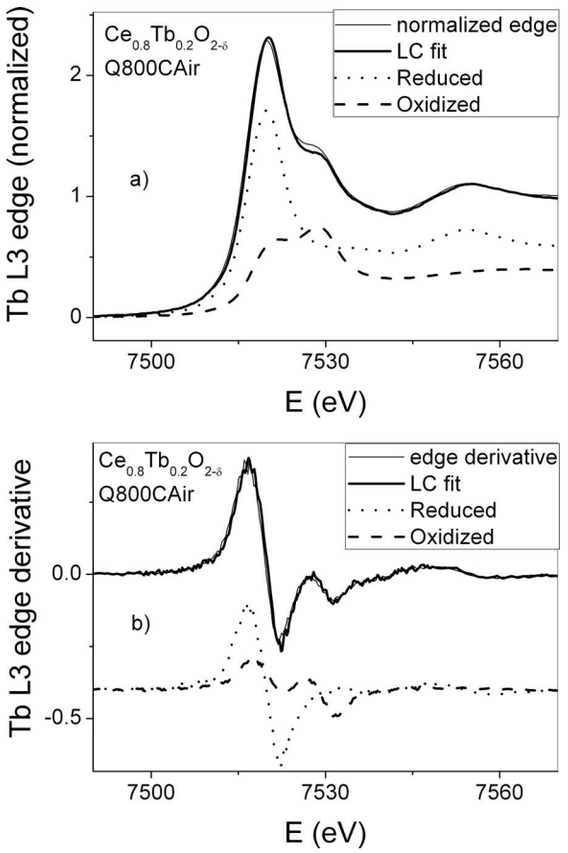

Figure 5. LC fit of (a) the L3 absorption edge of Tb for $Ce_{0.8}Tb_{0.2}O_{2-\delta}$ quenched from 800°C in air and (b) its first derivative.

types of neighbors, and local symmetries as in the examined material can be used. A mean value of the oxidation state of each element in the Q800CAir samples was estimated by LC fitting of the L3 absorption edge and its derivative, using the spectra of the Reduced and Oxidized samples as references. As an example, the LC fit of the absorption edge and the derivative of $Ce_{0.8}Tb_{0.2}O_{2-\delta}$ are shown in Fig. 5a and b, respectively. χ^2 values below 0.02 were obtained in all cases, indicative of a very good fit. It should be stressed that only one parameter was varied to obtain the fit, the relative weight of the reference spectra, directly giving the relative amount of each valence state.

The relative fraction of tetravalent Pr and Tb, estimated in this manner, is shown in Fig. 6 as a function of the concentration of Pr, the total amount of doping being 20 atom % in all cases. The fit of the absorption and the derivative of the absorption spectra gave very similar results. It can be seen that the tetravalent fraction of each dopant depends on the relative concentration of the co-dopant, increasing for Tb with an increasing amount of Pr and decreasing for Pr with increasing Tb concentration. The same trend was observed when using the edge shift or the ratio of the integrated intensities of peaks A and B as an indication of the tetravalent dopant fraction.

The observed dependence of the redox properties of Pr/Tb on the concentration of the co-dopant can be rationalized on the basis of minimization of the lattice strain energy by matching the average ionic radius of the dopants to that of the host. The presence of the voluminous Pr stabilizes the tetravalent state of Tb as a means of relaxing the strain in the lattice, stemming from the host–dopant mismatch. However, Tb, having a smaller ionic radius than Ce, tends to stabilize the trivalent state of Pr. The values of the ionic radii discussed are given in Table II.[37] Other studies have also shown a correlation between the redox properties of Pr and Tb in

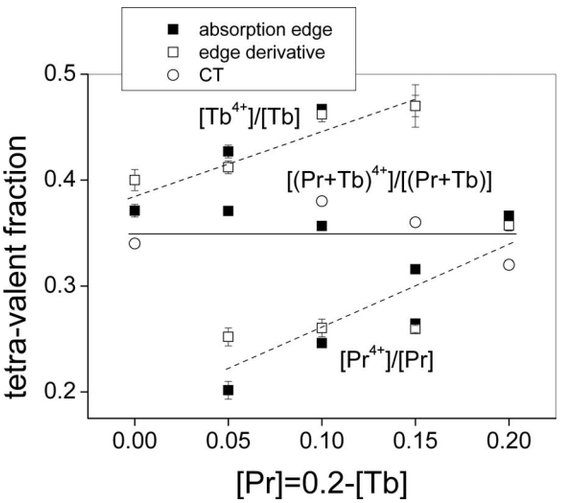

Figure 6. Fraction of tetravalent Pr and Tb and total tetravalent dopant fraction as determined from XANES for Q800CAir samples and CT at 800°C in air. The lines are a guide for the eyes.

ceria with the amount and type of doping or co-doping.[13,18,24,30,31] Minimization of the lattice strain energy can account for most of the observed dependencies, such as the increase in the trivalent fraction of Tb or Pr when co-doping with Zr and the increase in the tetravalent fraction of Tb when co-doping with Ca.

The overall tetravalent dopant fraction, as determined from XANES for the Q800CAir samples, remains constant within experimental uncertainty, as shown in Fig. 6. Good agreement is observed between the values obtained from XANES and CT at 800°C in air, validating the analysis and the quantification of the oxidation states deduced from the absorption spectra.

The relative tetravalent fraction of Tb in $Ce_{0.8}Tb_{0.2}O_{2-\delta}$, as determined by CT at 700, 800, and 900°C, is compared to that of $TbO_{2-\delta}$ [48] at the same temperatures and P_{O_2} range (Fig. 7). The tetravalent fraction of Tb decreases much faster with decreasing P_{O_2} in $Ce_{0.8}Tb_{0.2}O_{2-\delta}$ than in $TbO_{2-\delta}$ at all temperatures. This is in accordance with the speculated facilitated reduction of Tb in the lattice of ceria for reasons of minimization of the lattice strain energy.

Thermal and chemical expansion.— The strain, $\Delta L/L_0$, and TEC, $a = d(\Delta L/L_0)/dT$, measured upon cooling specimens of the

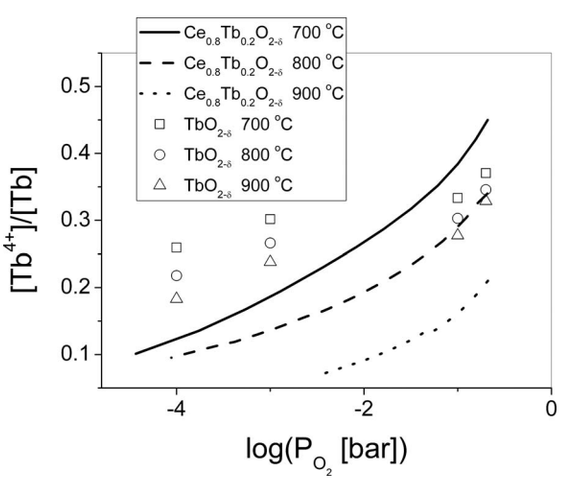

Figure 7. Comparison of tetravalent fraction of Tb in $TbO_{2-\delta}$ and $Ce_{0.8}Tb_{0.2}O_{2-\delta}$ at 700, 800, and 900°C as a function of P_{O_2}.

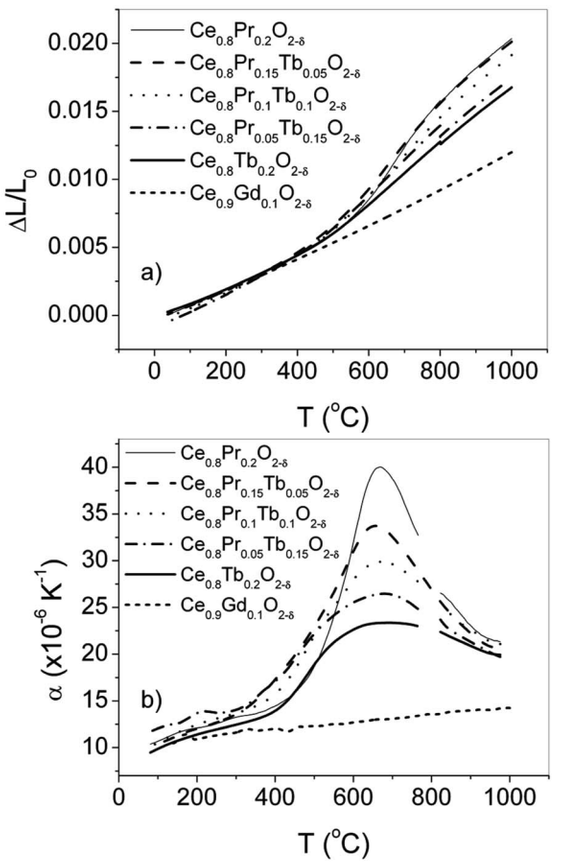

Figure 8. (a) Strain and (b) TEC as a function of temperature in air.

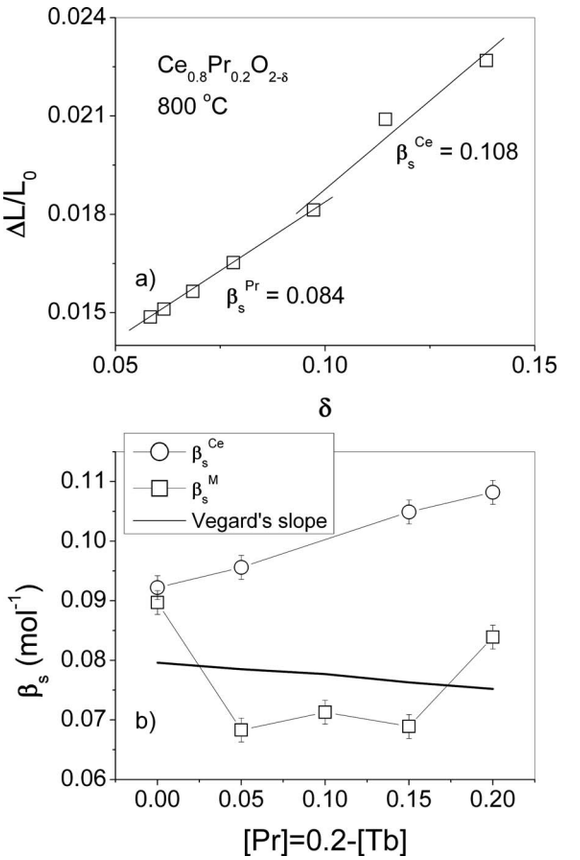

Figure 9. (a) Chemical strain as a function of oxygen nonstoichiometry for $Ce_{0.8}Pr_{0.2}O_{2-\delta}$ at 800°C and (b) chemical expansion coefficients due to reduction of Pr/Tb and of Ce as a function of Pr concentration. The dashed lines are a guide for the eyes.

various compositions from 1000°C to room temperature are presented in Fig. 8a and b, respectively. Apart from $Ce_{0.9}Gd_{0.1}O_{1.95}$, all compositions demonstrate a nonlinear strain behavior with an inflection point at around 650°C (i.e., a maximum in the TEC, Fig. 8b). This highly nonlinear behavior is attributed to the contribution of thermally induced chemical strain arising from the changing oxygen nonstoichiometry with temperature in air.

The maximum TEC value increases with increasing concentration of Pr, reaching a value of 40×10^{-6} K^{-1} for $Ce_{0.8}Pr_{0.2}O_{2-\delta}$, which agrees with a reported value of $\sim 36 \times 10^{-6}$ K^{-1}.[18] The observed peak becomes sharper with an increasing relative concentration of Pr. Both observations are related to the larger $d\delta/dT|_{P_{O_2}=\text{const}}$ slope of the Pr-rich compositions (Fig. 2) in air, which leads to a faster increase in chemical strain. The integrated TEC increases with an increasing concentration of Pr from 18.2×10^{-6} to 22.7×10^{-6} K^{-1} in the temperature range of 100–950°C (Table III).

Table III. Integrated thermal expansion and chemical expansion coefficients.

[Pr] = 0.20 − [Tb]	a_{int} (100–950°C) ($\times 10^{-6}$ K^{-1})	β_s^M (mol^{-1})	β_s^{Ce} (mol^{-1})
0.20	22.7	0.084	0.108
0.15	22.5	0.069	0.105
0.10	21.0	0.071	—
0.05	18.9	0.068	0.096
0.00	18.2	0.090	0.092
CGO10	12.5	—	—

The chemical strain of $Ce_{0.8}Pr_{0.2}O_{2-\delta}$ is shown in Fig. 9a as a function of oxygen nonstoichiometry at 800°C. The slope of $(\Delta L/L_0)(\delta)$ with respect to δ yields the chemical expansion coefficient, β_s. As can be seen in Fig. 9a, the slope changes at $\delta \approx 0.1$. The value of β_s for $\delta < 0.1$ corresponds to the chemical expansion coefficient resulting from the reduction of the dopants, whereas the value of β_s for $\delta > 0.1$ is related to the reduction of Ce. The chemical expansion coefficients related to the reduction of the dopants and Ce determined at 800°C are plotted in Fig. 9b as a function of the concentration of Pr. The continuous line corresponds to the value of Vegard's slope, estimated from Kim's empirical relation[36] using the ionic radii given in Table II. Although the determined values of β_s^M are very similar to the estimated values of Vegard's slope, β_s^M is observed to acquire lower values for the co-doped compositions, whereas Vegard's slope predicts a slow linear decrease in β_s^M with increasing Pr concentration. This is probably related to the enhanced flexibility of the co-doped compositions to adjust their redox properties to minimize the lattice strain, as concluded from the XANES results. The chemical expansion coefficient related to the reduction of Ce, β_s^{Ce}, is slightly larger than the one related to the reduction of the dopants and linearly increases with increasing Pr concentration. Values of the chemical expansion coefficients are listed in Table III.

Having determined the value of the chemical expansion coefficient related to the reduction of the dopants, β_s^M, the chemical strain induced upon changing the temperature in air can be estimated from

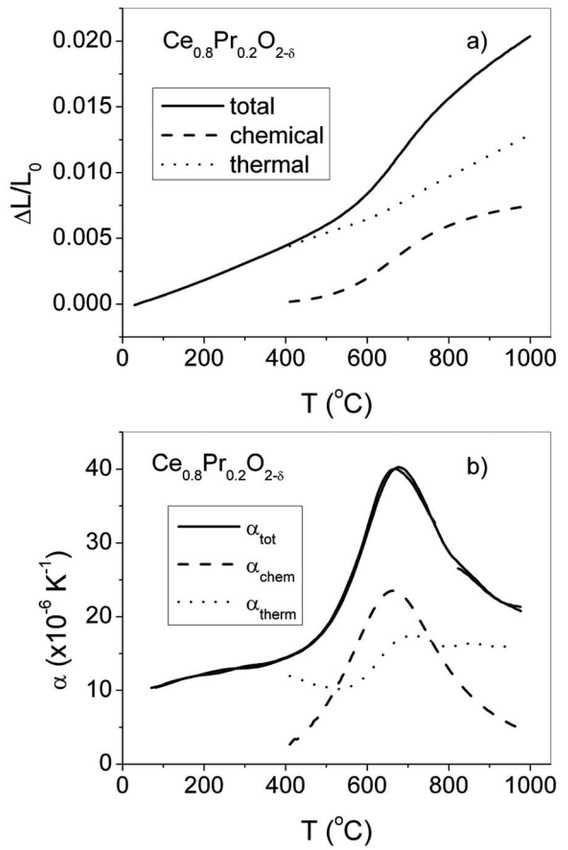

Figure 10. Deconvolution of (a) total strain upon temperature change and (b) TEC into their chemical and thermal components.

$$\left(\frac{\Delta L}{L_0}\right)_{\text{chem}}(T) = \beta_s^{\text{M}} \cdot \delta(T) \qquad [9]$$

The temperature dependence of the oxygen nonstoichiometry in air can be estimated from the thermodynamic parameters obtained from the fit of the $\delta(\log P_{O_2})$ data with the δ-linear solution model. The deconvolution of the total strain, induced on $Ce_{0.8}Pr_{0.2}O_{2-\delta}$ upon heating from room temperature to 1000°C in air, into its chemical and thermal components is shown in Fig. 10a. The thermal component is simply obtained by subtracting the chemical component from the measured total strain.

Differentiation with respect to temperature yields the chemical and thermal contributions to the TEC. These are shown in Fig. 10b. Values of a_{tot} determined both during heating and cooling are presented and are almost identical. This indicates that the specimen was always close to equilibrium during the heating and cooling ramps. The temperature at which the maximum in a_{chem} is estimated matches very well with the temperature where the maximum in a_{tot} is observed. It can also be seen that the shape of a_{chem} matches very well with the shape of the peak of a_{tot}. These are clear indications that the nonlinear behavior of the TEC originates from thermally induced chemical strain. a_{therm} increases from $\sim 11 \times 10^{-6}$ K^{-1} at low temperatures to $\sim 16 \times 10^{-6}$ K^{-1} at high temperatures, with a sharp increase observed at the region where the reduction of Pr proceeds at a fast rate. The increase in a_{therm} should therefore be primarily attributed to the decreasing metal–oxygen bond strength upon reduction of the dopants. An increase in the value of the TEC is generally observed in rare-earth-doped cerias upon increasing the dopant content or ionic radius.[49-51] The TEC of CeO_2 has been reported to increase from 11.7×10^{-6} K^{-1} for the undoped composition to 15.0×10^{-6} and 16.4×10^{-6} K^{-1} for the 20 atom % La- and Bi-doped compounds, respectively,[52,53] a similar change in magnitude to that observed here.

Conclusion

The oxygen nonstoichiometry of $Ce_{0.8}Pr_xTb_{0.2-x}O_{2-\delta}$ (x = 0, 0.05, 0.10, 0.15, 0.20) was measured as a function of P_{O_2} at temperatures between 600 and 900°C by CT and TG. A nonideal solution model allowing for a linear δ dependence of the partial molar enthalpy for the reduction of the dopants could successfully account for the measured $\delta(\log P_{O_2})$ data. In the fully oxidized state, Tb is more readily reduced in the lattice of ceria than Pr. The partial molar enthalpy for the reduction of the dopants decreases with increasing oxygen nonstoichiometry for the Pr-rich compositions, resulting in an easier release of oxygen from the lattice, whereas it remains unaffected for the Tb-rich compositions.

The valence states of Ce, Pr, and Tb in $Ce_{0.8}Pr_xTb_{0.2-x}O_{2-\delta}$ solid solutions, quenched from 800°C in air, were determined by XANES at the L3 edge of each element. The oxidation state of Pr and Tb depended on the relative amount of the two dopants. The tetravalent fraction of Tb increased with increasing relative concentration of Pr, whereas the tetravalent fraction of Pr decreased with increasing relative concentration of Tb. This behavior is attributed to the minimization of the lattice strain energy, as further supported by reported results. The overall tetravalent dopant fraction determined from XANES remained approximately constant for all compositions and agreed with values determined by CT at 800°C in air.

The thermal and chemical expansion coefficients have been determined from dilatometry measurements. A strong nonlinear behavior was observed in the TEC, which originates from chemical strain due to increasing oxygen nonstoichiometry with increasing temperature. The co-doped materials show a smaller chemical strain on reduction than the end members, $Ce_{0.8}Tb_{0.2}O_{2-\delta}$ and $Ce_{0.8}Pr_{0.2}O_{2-\delta}$.

Acknowledgments

Financial support from the Danish Council for Strategic Research, Programme Commission on Sustainable Energy and Environment, project no. 2104-0450041, is gratefully acknowledged. The authors thank K. Klementiev for a valuable experimental assistance at the beam line and HASYLAB for providing beam time within the project II-04-001EC.

Risø DTU, National Laboratory for Sustainable Energy assisted in meeting the publication costs of this article.

References

1. B. C. H. Steele, *Solid State Ionics*, **134**, 3 (2000).
2. A. Trovarelli, *Catal. Rev. - Sci. Eng.*, **38**, 439 (1996).
3. O. Yamamoto, in *Solid State Electrochemistry*, P. G. Bruce, Editor, p. 292, Cambridge University, Cambridge, MA (1995).
4. M. Stoukides, *Catal. Rev. - Sci. Eng.*, **42**, 1 (2000).
5. R. N. Blumenthal and P. J. Panlener, *J. Phys. Chem. Solids*, **31**, 1190 (1970).
6. R. N. Blumenthal and R. L. Hofmaier, *J. Electrochem. Soc.*, **121**, 126 (1974).
7. H. L. Tuller and A. S. Nowick, *J. Phys. Chem. Solids*, **38**, 859 (1977).
8. I. K. Naik and T. Y. Tien, *J. Phys. Chem. Solids*, **39**, 311 (1978).
9. E. Ruiz-Trejo and J. Maier, *J. Electrochem. Soc.*, **154**, B583 (2007).
10. B. Dalslet, P. Blennow, P. V. Hendriksen, N. Bonanos, D. Lybye, and M. Mogensen, *J. Solid State Electrochem.*, **10**, 547 (2006).
11. T. S. Stefanik and H. L. Tuller, *J. Electroceram.*, **13**, 799 (2004).
12. P. Shuk and M. Greenblatt, *Solid State Ionics*, **116**, 217 (1999).
13. D. P. Fagg, V. V. Kharton, A. Shaula, I. P. Marozau, and J. R. Frade, *Solid State Ionics*, **176**, 1723 (2005).
14. S. Lübke and H. D. Wiemhöfer, *Solid State Ionics*, **117**, 229 (1999).
15. P. Shuk, M. Greenblatt, and M. Croft, *Chem. Mater.*, **11**, 473 (1999).
16. X. Qi, Y. S. Lin, C. T. Holt, and S. L. Swartz, *J. Mater. Sci.*, **38**, 1073 (2003).
17. C. Ftikos, M. Nauer, and B. C. H. Steele, *J. Eur. Ceram. Soc.*, **12**, 267 (1993).
18. D. P. Fagg, I. P. Marozau, A. L. Shaula, V. V. Kharton, and J. R. Frade, *J. Solid State Chem.*, **179**, 3347 (2006).
19. C. Chatzichristodoulou and P. V. Hendriksen, *J. Electrochem. Soc.*, Accepted for publication.
20. J. Mizusaki, S. Yamauchi, K. Fueki, and A. Ishikawa, *Solid State Ionics*, **12**, 119 (1984).
21. J. Mizusaki, Y. Mima, S. Yamauchi, K. Fueki, and H. Tagawa, *J. Solid State Chem.*, **80**, 102 (1989).
22. S. Onuma, K. Yashiro, S. Miyoshi, A. Kaimai, H. Matsumoto, Y. Nigara, T.

Kawada, J. Mizusaki, K. Kawamura, N. Sakai, et al., *Solid State Ionics*, **174**, 287 (2004).
23. E. Bakken, S. Stølen, T. Norby, R. Glenne, and M. Budd, *Solid State Ionics*, **167**, 367 (2004).
24. D. P. Fagg, J. R. Frade, V. V. Kharton, and I. P. Marozau, *J. Solid State Chem.*, **179**, 1469 (2006).
25. F. Ye, T. Mori, D. R. Ou, J. Zou, and J. Drennan, *J. Nanosci. Nanotechnol.*, **7**, 2521 (2007).
26. K. J. de Vries and G. Y. Meng, *Mater. Res. Bull.*, **33**, 357 (1998).
27. A. B. Hungría, A. Martínez-Arias, M. Fernández-García, A. Iglesias-Juez, A. Guerrero-Ruiz, J. J. Calvino, J. C. Conesa, and J. Soria, *Chem. Mater.*, **15**, 4309 (2003).
28. A. Martínez-Arias, A. B. Hungría, M. Fernández-García, A. Iglesias-Juez, J. C. Conesa, G. C. Mather, and G. Munuera, *J. Power Sources*, **151**, 43 (2005).
29. X. Wang, J. C. Hanson, G. Liu, J. A. Rodriguez, A. Iglesias-Juez, and M. Fernández-García, *J. Chem. Phys.*, **121**, 5434 (2004).
30. X. Wang, J. C. Hanson, J. A. Rodriguez, C. Belver, and M. Fernández-García, *J. Chem. Phys.*, **122**, 154711 (2005).
31. M. Fernández-García, X. Wang, C. Belver, A. Iglesias-Juez, J. C. Hanson, and J. A. Rodriguez, *Chem. Mater.*, **17**, 4181 (2005).
32. J. Rodríguez-Carvajal, *Physica B*, **192**, 55 (1993).
33. E. A. Stern and K. Kim, *Phys. Rev. B*, **23**, 3781 (1981).
34. K. Lu and E. A. Stern, *Nucl. Instrum. Methods Phys. Res.*, **212**, 475 (1983).
35. B. Ravel and M. Newville, *J. Synchrotron Radiat.*, **12**, 537 (2005).
36. D. J. Kim, *J. Am. Ceram. Soc.*, **72**, 1415 (1989).
37. R. D. Shannon, *Acta Crystallogr., Sect. A: Cryst. Phys., Diffr., Theor. Gen. Crystallogr.*, **32**, 751 (1976).
38. F. W. Poulsen, in *Proceedings of the Nordic Workshop on High Temperature Electrode Materials*, F. W. Poulsen, E. Ahlgren, and A. Holt, Editors, Risø, National Laboratory for Sustainable Energy, Roskilde, Denmark, p. 6 (1992).
39. G. Brouwer, *Philips Res. Rep.*, **9**, 366 (1954).
40. A. V. Soldatov, T. S. Ivanchenko, S. D. Longa, A. Kotani, Y. Iwamoto, and A. Bianconi, *Phys. Rev. B*, **50**, 5074 (1994).
41. A. Bianconi, A. Marcelli, H. Dexpert, R. Karnatak, A. Kotani, T. Jo, and J. Petiau, *Phys. Rev. B*, **35**, 806 (1987).
42. E. Alleno, C. Godart, B. Fisher, J. Genossar, L. Patlagan, and G. M. Reisner, *Physica B*, **259–261**, 530 (1999).
43. M. Sikora, C. Kapusta, K. Knížek, Z. Jirák, C. Autret, M. Borowiec, C. J. Oates, V. Procházka, D. Rybicki, and D. Zajac, *Phys. Rev. B*, **73**, 094426 (2006).
44. K. R. Pedersen and J. E. Jorgensen, *Physica C*, **264**, 185 (1996).
45. J. W. Sobczak, E. Sobczak, A. Drelinkiewicz, M. Hasik, and E. Wenda, *J. Alloys Compd.*, **362**, 162 (2004).
46. I. Arčon, J. Kolar, A. Kodre, D. Hanžel, and M. Strlič, *X-Ray Spectrom.*, **36**, 199 (2007).
47. T. Ressler, J. Wong, J. Roos, and I. L. Smith, *Environ. Sci. Technol.*, **34**, 950 (2000).
48. C. H. Yo, K. S. Ryu, E. S. Lee, and K. H. Kim, *Bull. Korean Chem. Soc.*, **15**, 33 (1994).
49. T. Hisashige, Y. Yamamura, and T. Tsuji, *J. Alloys Compd.*, **408–412**, 1153 (2006).
50. S. Wang, E. Oikawa, and T. Hashimoto, *J. Electrochem. Soc.*, **151**, E46 (2004).
51. H. Hayashi, M. Kanoh, C. J. Quan, H. Inaba, S. Wang, M. Dokiya, and H. Tagawa, *Solid State Ionics*, **132**, 227 (2000).
52. S. Dikmen, P. Shuk, and M. Greenblatt, *Solid State Ionics*, **126**, 89 (1999).
53. S. Dikmen, P. Shuk, and M. Greenblatt, *Solid State Ionics*, **112**, 299 (1998).